PNAS RESEARCH ARTICLE | NEUROSCIENCE

Nonquantal transmission at the vestibular hair cell–calyx synapse: K_{LV} currents modulate fast electrical and slow K^+ potentials

Aravind Chenrayan Govindaraju[a,b], Imran H. Quraishi[c], Anna Lysakowski[d], Ruth Anne Eatock[e], and Robert M. Raphael[b,1]

Edited by Robert Fettiplace, University of Wisconsin-Madison, Madison, WI; received May 1, 2022; accepted November 17, 2022

Vestibular hair cells transmit information about head position and motion across synapses to primary afferent neurons. At some of these synapses, the afferent neuron envelopes the hair cell, forming an enlarged synaptic terminal called a calyx. The vestibular hair cell–calyx synapse supports a mysterious form of electrical transmission that does not involve gap junctions, termed nonquantal transmission (NQT). The NQT mechanism is thought to involve the flow of ions from the presynaptic hair cell to the postsynaptic calyx through low-voltage-activated channels driven by changes in cleft $[K^+]$ as K^+ exits the hair cell. However, this hypothesis has not been tested with a quantitative model and the possible role of an electrical potential in the cleft has remained speculative. Here, we present a computational model that captures experimental observations of NQT and identifies features that support the existence of an electrical potential (ϕ) in the synaptic cleft. We show that changes in cleft ϕ reduce transmission latency and illustrate the relative contributions of both cleft $[K^+]$ and ϕ to the gain and phase of NQT. We further demonstrate that the magnitude and speed of NQT depend on calyx morphology and that increasing calyx height reduces action potential latency in the calyx afferent. These predictions are consistent with the idea that the calyx evolved to enhance NQT and speed up vestibular signals that drive neural circuits controlling gaze, balance, and orientation.

ephaptic transmission | synapse | vestibular | hair cells | computational neuroscience

Significance

The ability of the vestibular system to drive the fastest reflexes in the nervous system depends on rapid transmission of mechanosensory signals at vestibular hair cell synapses. In mammals and other amniotes, afferent neurons form unusually large calyx terminals on certain hair cells, and communication at these synapses includes nonquantal transmission (NQT), which avoids the synaptic delay of quantal transmission. We present a quantitative model that shows how NQT depends on the extent of the calyx covering the hair cell and attributes the short latency of NQT to changes in synaptic cleft electrical potential caused by current flowing through open potassium channels in the hair cell. This mechanism of electrical transmission between cells may act at other synapses.

The vestibular inner ear transduces head motion and drives the fastest known reflexes in the nervous system. These reflexes support gaze, balance, and orientation (1) and are essential for locomotion. The first synapses in these pathways are from mechanosensory hair cells onto primary afferent nerve terminals. In mammals and other amniotes, many vestibular afferent terminals form prominent cup-like structures, termed calyces, around specialized type I hair cells (2–4). Transmission at these synapses has been inferred to be exceptionally fast (5), prompting speculation that it includes a direct electrical component in addition to glutamate exocytosis from synaptic vesicles [quantal transmission (QT)]. Electrical transmission typically involves gap junctions (6), but gap junctions are not present at vestibular hair cell–calyx (VHCC) synapses (3). Nonetheless, electrophysiological recordings from calyx-bearing afferents established that an additional mode of transmission can occur, either with or without QT (7–11). This mysterious form of transmission came to be called Nonquantal Transmission (NQT).

NQT is thought to be mediated by the flow of ions from the presynaptic hair cell to the postsynaptic calyx through low-voltage-activated K^+ (K_{LV}) channels (12, 13), but how presynaptic currents alter the driving forces of postsynaptic currents has not been well understood. A key challenge for understanding NQT at the VHCC synapse is the lack of direct experimental access to the synaptic cleft and pre- and postsynaptic membranes. Early models (14, 15) recognized that the elongated cleft space between the type I hair cell and enveloping calyx structure could provide increased electrical resistance and limit the diffusion of ions. In these formulations, K^+ that enters hair cells during mechanotransduction is extruded into the synaptic cleft, leading to K^+ accumulation and a change in the K^+ chemical potential that drives membrane currents. Changes in cleft electrical potential were not thought to be significant. In support of these models, subsequent experimental results emphasized the role of K^+ accumulation (11, 16–19). Other processes were also suggested, including accumulation of glutamate following quantal release (20) and proton extrusion from hair cells (10). However, the existence and role of an electrical potential in the synaptic cleft have remained matters of speculation. A clear biophysical explanation for how NQT occurs and how currents and driving forces interact quantitatively at the VHCC synapse has not yet been presented.

Author contributions: R.A.E. and R.M.R. designed research; A.C.G., I.H.Q., A.L., R.A.E., and R.M.R. performed research; R.A.E. analyzed data; and A.C.G., A.L., R.A.E., and R.M.R. wrote the paper.

The authors declare no competing interest.

This article is a PNAS Direct Submission.

[1]To whom correspondence may be addressed. Email: rraphael@rice.edu.

This article contains supporting information online at https://www.pnas.org/lookup/suppl/doi:10.1073/pnas.2207466120/-/DCSupplemental.

Published January 3, 2023.

To elucidate the biophysical basis of NQT, we have developed a detailed computational model of the VHCC synapse based on the anatomy of the afferent calyx terminal and the properties of ion channels and transporters expressed in the hair cell, calyx terminal, and afferent fiber. Simulated responses of the VHCC model to hair bundle deflection and voltage-clamp steps accurately predict experimental data. Such validation gives us confidence in the model's predictions for sites with limited experimental data, notably the inaccessible synaptic cleft. Results show that NQT at the VHCC synapse depends on the geometry of the calyx, involves modulation of both the electrical potential and K^+ concentration in the synaptic cleft, and is mediated primarily by currents through K_{LV} conductances that take different forms in the presynaptic and postsynaptic membranes ("$g_{K,L}$" channels and K_V7 channels, respectively). A major outcome of the model is the recognition of features in postsynaptic responses (9, 18) as evidence for changes in electrical potential in the synaptic cleft during NQT.

Changes in extracellular electrical potential have long been known to play a role in ephaptic coupling, a general term for coupling via proximity of neural elements (6, 21). Ephaptic coupling has been implicated in signal transmission in the retina (22, 23), cerebellum (24), hippocampus (25), and heart (26). At the VHCC synapse, however, the importance of changes in cleft electrical potential has gone unrecognized despite its extensive synaptic cleft, which is formed by the close apposition of the presynaptic (hair cell) and postsynaptic (afferent) membranes. The VHCC model we develop is able to decouple electrical and K^+ potentials and demonstrate that change in cleft electrical potential is necessary to explain: 1) the short latency of NQT; 2) the experimentally observed phase response of NQT (9); 3) fast retrograde events in the hair cell during postsynaptic action potentials (APs) (11); and 4) the shape of the fast current response of the calyx to voltage changes in the hair cell (18). By showing how the magnitude and speed of NQT depend on the calyx, our model supports the idea that the calyx evolved to support faster transmission in response to increased locomotory challenges presented by the tetrapod transition from water to land (12, 27).

Abbreviations

Electrical potentials (with respect to perilymph):
ϕ_H electric potential in the hair cell
ϕ_{SC} electric potential in the synaptic cleft
ϕ_C electric potential in calyx
Transmembrane voltages
V_H voltage across the basolateral hair cell membrane, $(\phi_H - \phi_{SC})$
V_{CIF} voltage across calyx inner face membrane, $(\phi_C - \phi_{SC})$
Concentrations and ionic potentials
$[K^+]_{SC}$ K^+ concentration in the synaptic cleft
$[Na^+]_{SC}$ Na^+ concentration in the synaptic cleft
E_K Equilibrium potential for K^+ (K^+ potential) across hair cell or calyx membranes

General Description of the Model

The model has been developed for an afferent calyx around a single type I hair cell ("simple calyx-only terminal") based on the geometry of a vestibular hair cell and calyx from the striolar zone of the rat utricle, see Fig. 1 and *SI Appendix*, Fig. S1. The morphology of vestibular hair cells and calyces is highly conserved within particular zones of vestibular epithelia (28, 29), and thus the model is representative of "simple" VHCC synapses in the striolar zone.

The model incorporates ion channels and transporters identified from experimental studies of type I hair cells and associated afferents to simulate the voltage response of the calyx to mechanical and electrical stimuli: hair bundle deflection and hair cell voltage steps. Most of the parameters in the model are from published literature (*SI Appendix*, Tables S5, S6, and S7); methods are provided for our experimental data (*SI Appendix*, Experimental Methods). The model was created to understand how ionic currents and driving forces interact at the VHCC synapse during NQT: a change in the calyx potential in response to a change in hair cell potential that involves neither exocytosis of packets (vesicles or quanta) of neurotransmitter nor gap junctions. As the goal is to understand NQT as an independent phenomenon, we do not consider QT. The predictions of the model are compared with experimental results from synapses that displayed only NQT. Simulations used physiological parameters from experimental data performed at room temperature.

The key parameters of interest are changes that occur in the electrical potential and K^+ concentration of the synaptic cleft, which are not directly experimentally measurable. The model incorporates capacitive and resistive currents across both the presynaptic hair cell and postsynaptic calyx membranes and uses continuity and electro-diffusion equations to describe the relationship between currents, electrical potentials, and ion concentrations in the synaptic cleft (31). Using a finite element approach and COMSOL Multiphysics® software, we simulate the effects of changes in electrical potential in each model compartment and how these changes represent the mechanosensory signal as it travels from one compartment to the next. In the synaptic cleft, spatiotemporal changes in both electrical potential and ion concentrations are simulated and show spatially varying driving forces for currents along the basal-to-apical extent of hair cell and calyx inner face membranes. Initial conditions, boundary conditions, and full details on channel kinetics are provided in *SI Appendix*. The overall geometry, localization of ion channels, and other relevant variables are presented in Fig. 1.

Results

We use the VHCC model to delineate biophysical events and driving forces that underlie NQT and describe how the mechanosensory signal is communicated to the calyx terminal of the afferent neuron. We first describe the resting state of the VHCC compartments, then responses to step bundle deflections. In each condition, we provide the model's output in terms of: 1) electrical potentials relative to a distant ground for the hair cell (ϕ_H), synaptic cleft (ϕ_{SC}), and calyx (ϕ_C); 2) transmembrane voltages for the hair cell (V_H) and the calyx inner face (V_{CIF}) membranes facing the synaptic cleft; 3) K^+ and Na^+ concentrations in the synaptic cleft ($[K^+]_{SC}$, $[Na^+]_{SC}$); and 4) key ion-channel currents across each membrane. The contributions of ϕ_{SC} and $[K^+]_{SC}$ are then analyzed separately to determine their roles in driving pre- and postsynaptic currents and thus NQT. We then compare model results with published data showing NQT during sinusoidal hair bundle displacement and paired voltage-clamp recordings from hair cells and calyces to identify features that corroborate the existence and role of an electrical potential in the cleft. Finally, to understand the extent to which NQT depends on calyx morphology, we analyze the effect of calyx height on the electrical and potassium potentials in the cleft (ϕ_{SC}, E_K) and the response latency of the calyx.

Resting State of the System. The model was fully defined with no free parameters that required additional estimation. From the initial values and boundary conditions, we calculated the resting currents, ion concentrations, electrical potentials, and membrane voltages, using the stationary solver in COMSOL (*SI Appendix*, Computational Methods). At rest, the MET (mechanoelectrical

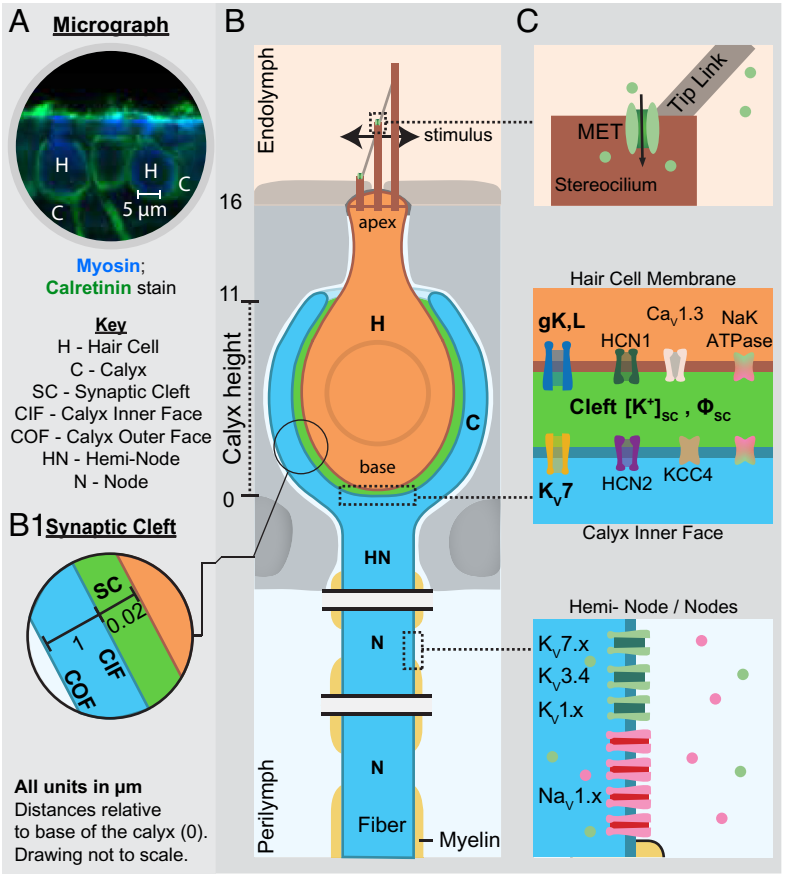

Fig. 1. Illustration of the VHCC synapse depicting the distribution of ion channels and transporters in the hair cell (H), synaptic cleft (SC), calyx (C), and afferent fiber (F). (*A*) Confocal micrograph of type I hair cells (H, *blue* myosin immunolabel) within calyces (C, *green* calretinin immunolabel). Long–Evans adult rat utricle, striolar zone. (*B*) Geometry of a type I hair cell-calyx synapse from central/striolar zones of rodent vestibular organs. A 2D curve representing the hair cell, synaptic cleft, and calyx was generated (*SI Appendix*, Fig. S1) based on measurements from Lysakowski et al. (30), their Fig. 2*C*. Long–Evans adult rat crista, central zone. Dimensions were comparable (within 10%) to those of hair cells and calyces in *A*. (*B*1) Cleft and calyx width. (*C*) The ion channel types at different key locations in the model. See *SI Appendix*, Tables S6 and S7 for sources of channel kinetics and distributions. ϕ_{SC}, electrical potential in the synaptic cleft; $[K^+]_{SC}$, K^+ concentration in the synaptic cleft.

transduction) channels had a 10% open probability, corresponding to –43 pA of current. The model produced hair cell and calyx resting potentials (ϕ_H: –78 mV, ϕ_C: –65 mV) that are consistent with reported resting ϕ_H and ϕ_C (20, 32–36). Model resting output values for which there are no experimental data for comparison are: ϕ_{SC} at the base of the synapse, +2 mV; $[K^+]_{SC}$ and $[Na^+]_{SC}$ at the base of the synapse, 7 mM and 129 mM, respectively. The nonzero value for ϕ_{SC} emerges from currents at rest carried by the same ion channels and transporters that participate in stimulus-evoked NQT.

These results were taken as the initial conditions from which to determine, with the time-dependent solver (COMSOL), changes in response to a stimulus. In all figures, the values at t = 0 show conditions at rest.

Synaptic Response to a Step Displacement of the Hair Bundle. In Fig. 2, we illustrate the simulated response of sequential stages in the VHCC model to a positive (excitatory) step (+1 µm) of hair bundle displacement at 50 ms followed by a negative (inhibitory) displacement (–1 µm). The stimulus (Fig. 2*A*) is bundle displacement viewed from above relative to resting position, taken mid-way up the bundle and parallel to the plane of the epithelium (Fig. 1*B*, "stimulus"). The mechanotransduction current (I_{MET}) elicited by bundle stimulation is shown in Fig. 2*B*. Positive bundle displacement evoked a peak inward I_{MET} of ~400 pA, and the negative step reduced I_{MET} to 0. These changes in I_{MET} depolarized and hyperpolarized ϕ_H (Fig. 2*C*, modeled by *SI Appendix*, Eq. **S2**), respectively, and altered hair cell basolateral (presynaptic) currents (Fig. 3). This model does not consider transducer adaptation, such that any decay (adaptation) of I_{MET} is driven by changes in ϕ_H, which changes the driving force on I_{MET}. NQT manifests as a change in calyx potential, ϕ_C (Fig. 2*G*), in response to changes in hair cell potential, ϕ_H. For this bundle deflection, the NQT-induced change in ϕ_C was large enough to trigger an AP in the calyx, which is in turn transmitted retrogradely by NQT back to the hair cell, showing up as transients at each stage (Fig. 2 *B*–*F*, arrowheads and Fig. 3 *A*–*C*, vertical dashed line and asterisks).

Predicted Changes in Cleft Electrical Potential, Na^+ and K^+ Concentrations and Transmembrane Voltages. The model permits dynamic simulation of biophysical properties of the cleft microenvironment as a function of spatial location. During NQT, the synaptic cleft potential at the base, ϕ_{SC} , changes as shown in Fig. 2 *E* and *E*1. The dynamic changes in ϕ_{SC} (modeled by *SI Appendix*, Eq. **S5**) allow calculation of presynaptic ($V_H = \phi_H - \phi_{SC}$) and postsynaptic ($V_{CIF} = \phi_C - \phi_{SC}$) transmembrane voltages. V_H (Fig. 2*D*) and V_{CIF} (Fig. 2*F*) differ by ϕ_{SC} from the intracellular potentials with respect to ground (ϕ_H and ϕ_C, Fig. 2 *C* and *G*).

Fig. 2*E* shows the predicted changes in $[K^+]_{SC}$ and $[Na^+]_{SC}$ in the synaptic cleft at its base: K^+ accumulation was accompanied by Na^+ depletion, as predicted by a previous electro-diffusion model of the

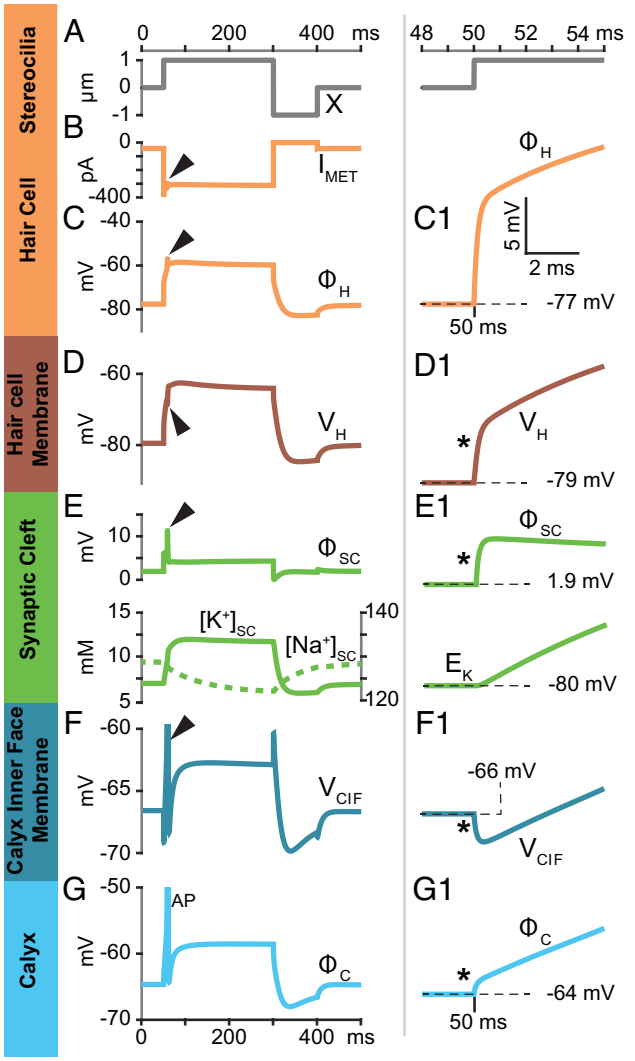

Fig. 2. Propagation of the mechanosensory signal evoked by hair bundle displacement, illustrating dynamic changes in electrical and K^+ potentials at each stage. (*A*) Displacement (X) of the hair bundle: +1 μm, 250-ms step, beginning at t = 50 ms and followed by negative step to −1 μm (300-ms) step. (*B–G*) Responses to full stimulus, progressing from (*B*) the mechanotransduction current I_{MET} to (*G*) the calyx postsynaptic potential ϕ_C. Arrowheads point to the retrograde echo of a calyx AP that was stimulated by anterograde transmission. (*C–G*) Values shown are at the base of the synapse. (*C1–G1*) Responses in *C–G* to +step on expanded time scale (between 48 and 55 ms). (*C* and *C1*) Hair cell receptor potential (electrical potential re: ground, ϕ_H) rises rapidly. (*D* and *D1*) Voltage across the basolateral hair cell membrane (V_H) rises rapidly but is smaller than ϕ_H by the cleft potential ($V_H = \phi_H - \phi_{SC}$). (*E*) *Top* row, Synaptic cleft electrical potential relative to ground (ϕ_{SC}); *Bottom* row, ion concentrations $[K^+]_{SC}$ (*solid line*; *Left* axis) rises while $[Na^+]_{SC}$ (*dotted line*; *Right* axis) falls. (*E1*) ϕ_{SC} *Top* row, rises much faster than K^+ potential (E_K) for $[K^+]_{SC}$, *Bottom* row. (*F* and *G*) Voltage across calyx inner face membrane ($V_{CIF} = \phi_C - \phi_{SC}$) rapidly hyperpolarizes (*F* and *F1*) and then reverses as ϕ_C depolarizes (*G* and *G1*), ultimately producing a calyceal AP (*G*). Note that after +step onset, fast components (*) of V_H (*D1*) and V_{CIF} (*F1*) have opposite polarities and same time course as the fast rise (*) in ϕ_{SC} (*E1*).

type I-calyx that considered the effect of the cleft on the hair cell receptor potential (37). In our VHCC model, changes in ion concentrations in the cleft are caused by: 1) altered ionic currents, mostly through channels in the presynaptic and postsynaptic membranes; and 2) the axial electro-diffusion of ions from the source (ion channels facing the cleft) to the sink (perilymph at the apical edges of the calyx) (Fig. 1 and *SI Appendix*, Eqs. **S3** and **S4**).

Synaptic Cleft Electrical Potential, ϕ_{SC}, Rises Much Faster than the Synaptic K^+ Potential. To more clearly illustrate the variables responsible for the speed of NQT, we show the dynamic changes in ϕ_H (Fig. 2*C*1) and ϕ_C (Fig. 2*G*1), V_H and V_{CIF} (Fig. 2 *D*1 and *F*1), and synaptic cleft potential, ϕ_{SC} (Fig. 2*E*1) at the onset of the +1-μm step. We also plot the equilibrium potential of K^+, (E_K), which reflects changes in synaptic cleft potassium level, $[K^+]_{SC}$ (Fig. 2*E*1).

Differences in the time courses of stimulus-evoked changes in ϕ_{SC}, E_K, and V_{CIF} provide key insight into the driving forces for NQT. At the onset of the positive step, the synaptic cleft potential, ϕ_{SC}, rises from 1.9 mV to +6 mV in 0.43 ms, eightfold faster than the time for E_K to rise the same amount (–79.9 mV to –75.8 mV) (Fig. 2*E*1). The rise in E_K is also slow compared with the change in V_{CIF} (Fig. 2*F*1). This provides an important insight into the mechanism of NQT that has not been previously recognized: ϕ_{SC} provides the initial driving force for change in the postsynaptic membrane current, and only later does change in E_K make a significant contribution. This difference arises because fewer ions are needed to change ϕ_{SC} than to change $[K^+]_{SC}$ and E_K (38); see *SI Appendix*, Notes. Fig. 2 (*C1–F1*) highlights how changes in ϕ_{SC} (Fig. 2*E*1) affect the magnitude of V_H (Fig. 2*D*1) and the magnitude and direction of V_{CIF} (Fig. 2*F*1). At step onset, V_{CIF} hyperpolarizes while ϕ_C depolarizes (Fig. 2 *F*1 and *G*1, asterisks). The hyperpolarization of V_{CIF} occurs because the fast depolarization of the cleft (ϕ_{SC}) is larger than the fast depolarization of the intracellular calyx potential (ϕ_C) making $V_{CIF} = (\phi_C - \phi_{SC})$ negative. The subsequent slow rise in V_{CIF} follows the depolarization of ϕ_C which results from the slow increase in $[K^+]_{SC}$ and E_K. That V_{CIF} and ϕ_C are different and can change in opposing directions makes it apparent that voltage across the calyx inner and outer face membranes can be different despite the common intracellular potential. While the VHCC model results agree with experiments showing that changes in $[K^+]_{SC}$ affect both hair cell and calyx signals (11, 16, 17, 19), the model further shows a pivotal role for the synaptic cleft potential in reducing transmission latency. The independent contributions of ϕ_{SC} and $[K^+]_{SC}$ to NQT are analyzed later.

Contributions of Different Ion Channels to NQT. The synaptic cleft is a dynamic system where electric potentials, ion concentrations, and ionic currents interact. The changes in cleft electrical potential and ion concentrations shown in Fig. 2 are driven by currents through voltage-sensitive ion channels (see *SI Appendix*, Table S6 for kinetics) on the hair cell basolateral membrane and on the calyx inner face, and in turn modulate these currents (Fig. 3). NQT is bidirectional: we first describe the roles of key channels during anterograde (hair cell to calyx) NQT and later discuss retrograde (calyx to hair cell) NQT.

Currents through Open $g_{K,L}$ Channels Respond Very Rapidly to Hair Cell Depolarization. The large low-voltage-activated K^+ conductance "$g_{K,L}$" is a distinctive feature of type I vestibular hair cells (32, 34, 39). At the resting bundle position (t < 50 ms, Figs. 2 and 3) before the step, V_H is only slightly positive (~1 mV) of E_K (–80 mV; Fig. 2*E*1). Despite this small driving force, $g_{K,L}$ carries significant outward K^+ current, $I_{K,L}$, into the cleft (Fig. 3*A*) because it has a large open probability (~50%) due to its very negative activation range and there are a large number of channels (35). At the onset of the positive step, ϕ_H and V_H depolarize faster than E_K (Fig. 2 *C*1–*E*1). Since $g_{K,L}$ is already significantly open, the increase in driving force ($V_H - E_K$) instantaneously increases $I_{K,L}$ (Fig. 3*A*), altering both ϕ_{SC} and, more gradually, $[K^+]_{SC}$. $I_{K,L}$ is largely sustained; a modest decrease (~10%, from +350 pA to +317 pA) reflects the reduction in driving force as $[K^+]_{SC}$ increases and E_K depolarizes (Fig. 3*B*).

In Fig. 3 we have presented local potentials at the base of the synapse and whole-cell ionic currents. However, the VHCC model

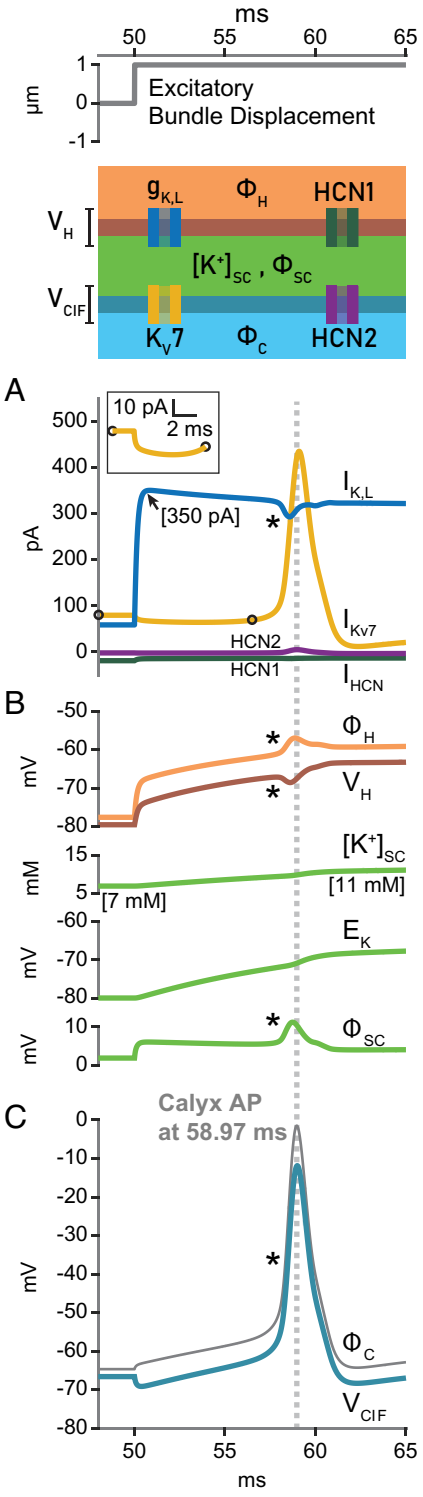

Fig. 3. Ionic currents during hair bundle stimulation and Retrograde NQT of a calyx AP to the hair cell. During excitatory step bundle displacements (*Top*), ionic currents (*A*), primarily through hair cell $g_{K,L}$ and calyx K_V7, are affected by and affect cleft properties (ϕ_{SC} and $[K^+]_{SC}$ in *B*). Anterograde NQT evokes a single AP in the calyx (*gray line, C*; peak shown by *dashed line*). Asterisks in *A–C* show the retrograde influence of the calyx AP on hair cell and calyx currents (*A*), hair cell and cleft properties (*B*), and calyx (*C*) voltages. (*A*) Net currents through $g_{K,L}$ (hair cell, *blue*), K_V7 (calyx, *gold*) and HCN channels (hair cell, *brown*, and calyx, *purple*) in response to the first 15 ms of the +1-μm step. (*A*) *inset*, expanded view of K_V7 current decrease at + step onset. (*B*) ϕ_H, V_H, $[K^+]_{SC}$, E_K and ϕ_{SC} at the base of the synapse during excitatory stimulus, showing that fast retrograde transmission to the hair cell occurs through ϕ_{SC} and not E_K. See asterisks. (*C*) V_{CIF} (*cyan*) and ϕ_C (*gray*, featuring the calyx AP) at the base of the synapse during excitatory stimuli.

has the ability to calculate the spatiotemporal distributions of these variables. In our model conditions, the net $I_{K,L}$ was never inward (negative). However, using the model to examine membrane currents as functions of location along the cleft, we noticed that inward $I_{K,L}$ can occur locally at the base of the hair cell during a negative step if V_H becomes negative to E_K (*SI Appendix*, Fig. S2). These results support the idea that $g_{K,L}$ may under certain conditions carry inward K^+ currents into the hair cell and aid in K^+ clearance (19).

Fig. 3 shows that the current through $g_{K,L}$ is fast, large, and noninactivating, allowing it to closely follow the hair bundle stimulus. Since $g_{K,L}$ is high in the resting state, the receptor potential-induced change in $I_{K,L}$ is not delayed by ion channel activation and is near-instantaneous. $I_{K,L}$ rapidly changes the cleft electrical potential (Fig. 3*B*, *Bottom trace*), which in turn rapidly alters currents through low-voltage-activated potassium (K_{LV}) channels in the calyx inner face membrane.

Excitatory Stimuli Decrease K_V7 Current into the Synaptic Cleft from the Calyx. The postsynaptic K_{LV} conductances include the K_V7 family of voltage-gated channels (40). The VHCC model permits quantitative characterization of the role of these channels in modulating $[K^+]_{SC}$ and ϕ_{SC} during NQT, which has not previously been clear. According to the model, at resting membrane potential (V_{CIF} = –68 mV), outward current through partly open (29%) K_V7 channels on the calyx inner face supplies K^+ to the synaptic cleft, helping to set resting levels of $[K^+]_{SC}$ and ϕ_{SC}. During positive bundle displacement, changes in V_{CIF} and E_K across the calyx inner face membrane (Fig. 3*B*) slightly reduce outward K_V7 currents into the synaptic cleft (Fig. 3*A*, I_{Kv7}, inset) except during the calyx AP where outward K_V7 currents increase (Fig. 3*A*, I_{Kv7}, asterisk).

Synaptic HCN Channels Establish Resting Conditions but Have Minimal Effect on $[K^+]_{SC}$ and ϕ_{SC} during NQT. Hyperpolarization-activated cyclic-nucleotide-gated (HCN) channels are found on both sides of the VHCC synapse. Type I hair cells primarily express HCN1 channel subunits (41), and vestibular afferent neurons primarily express HCN2 subunits (42). Model results show that under physiological concentrations and potentials, HCN channels support a net inward current in both cells, mediated by influx of Na^+ ions, that is 10 to 100-fold smaller than outward K^+ currents through $g_{K,L}$ and K_V7 channels (Fig. 3*A*). In the model, we localized HCN1 to the hair cell and HCN2 to the calyx and found that both HCN channels had smaller open probabilities (HCN1 - 18%; HCN2 - 8%) than K_{LV} channels ($g_{K,L}$ - 50%; K_V7 - 29%) at rest (V_H = –79 mV; V_{CIF} = –68 mV) and contributed very small currents to either positive (Fig. 3*A*) or negative (*SI Appendix*, Fig. S2) bundle step responses. This difference relative to K_{LV}-associated currents is explained by the HCN channels' smaller whole-cell conductance values (*SI Appendix*, Table S6), their hyperpolarized voltage range of activation, and their mixed cationic currents (K^+ and Na^+) moving in opposite directions. In the model, both HCN1 and HCN2 channels, along with the Na^+/K^+-ATPase, contribute to the regulation of $[K^+]$ and $[Na^+]$ in the synaptic cleft (Fig. 2*E*). Blocking HCN channels blocks NQT (11), but only under conditions that artificially favor HCN channels, i.e., when the calyx was held at –100 mV, an unphysiological (substantially negative to E_K) condition at which most K_V7 channels would be closed and most HCN channels would be open.

Retrograde Transmission from Calyx to Hair Cell. The VHCC model naturally captures retrograde transmission (Fig. 2 *B–F*, arrowheads), defined as a change in hair cell potential caused by

a change in calyx potential. This is especially pronounced during NQT-induced postsynaptic APs that occur for sufficiently large hair bundle displacements. An AP in the fiber (Figs. 2*G* and 3*C*) causes the calyx inner face membrane to depolarize (Fig. 3*C*, V_{CIF}) and increases outward current, primarily through K_V7 channels (Fig. 3*A*; compare K_V7 and HCN2); ϕ_{SC} rises (Fig. 3*B*); V_H becomes more negative (Fig. 3*B*); outward K^+ currents from the hair cell, primarily through $g_{K,L}$ channels, decrease (Fig. 3*A*, see $I_{K,L}$ and HCN1); and the hair cell potential, ϕ_H, depolarizes (Fig. 2*C*, arrowhead; Fig. 3*B*). The fast component of retrograde transmission is mediated by changes in ϕ_{SC} and not E_K (Fig. 3, asterisks). These results indicate that fast retrograde events seen in electrophysiological recordings of the hair cell and calyx (11) are caused by changes in electrical potential in the synaptic cleft. It has been suggested that the bidirectional nature of NQT, which our VHCC model captures, could be used to modulate the sensitivity of both the calyx and the hair cell (43).

Role of the Synaptic Cleft in NQT: ϕ_{SC} and $[K^+]_{SC}$. The predictions of the VHCC model agree with experimental observations (11, 16–19) that support the hypothesis that K^+ currents through the basolateral membrane of the type I hair cell modulate $[K^+]_{SC}$ (14, 15) and change E_K to affect pre- and postsynaptic currents. The model further shows that modulation of ϕ_{SC} also alters both presynaptic and postsynaptic ionic currents but on a substantially faster time scale. What are the relative contributions of ϕ_{SC} and $[K^+]_{SC}$ to NQT? Are both mechanisms necessary? What advantages do they provide? To answer these questions, we use the VHCC model to isolate ϕ_{SC} and $[K^+]_{SC}$ during both step and sinusoidal bundle displacements.

Isolation of the Contributions of ϕ_{SC} and $[K^+]_{SC}$ during Step Bundle Displacements. We mathematically define two conditions: ϕ_{SC} modulation and $[K^+]_{SC}$ modulation. The ϕ_{SC} modulation-only condition is set by fixing $[K^+]_{SC}$ and $[Na^+]_{SC}$ at 5 mM and 140 mM, respectively, while ϕ_{SC} is allowed to vary as a function of ionic currents (*SI Appendix*, Eqs. **S8–S10**). The $[K^+]_{SC}$ modulation-only condition is set by fixing ϕ_{SC} at 0 mV and allowing $[K^+]_{SC}$ and $[Na^+]_{SC}$ to vary as functions of the ionic currents (*SI Appendix*, Eqs. **S11–S13**). Fig. 4 illustrates how ϕ_{SC} and $[K^+]_{SC}$ separately and together shape the calyx potential (Fig. 4 *A*1 and *A*2) at the onset of positive bundle displacements of different magnitudes. The ϕ_{SC} modulation reduced the latency of the calyx potential by 1.8 ms (0.3-μm step) and 1.5 ms (1-μm step).

Fig. 4. also shows that $[K^+]_{SC}$ modulation is responsible for the slow component of the rise in calyx potential. When ϕ_{SC} and $[K^+]_{SC}$ are allowed to vary concomitantly, both fast and slow components are seen. Comparing the rise of ϕ_C in the $[K^+]_{SC}$ -only and "Both" conditions clearly shows that change in ϕ_{SC} confers a ~1 to 2-ms advance to the calyx response. Thus, the modulation of ϕ_{SC} enables faster signal transmission between hair cell and calyx. The modulation of $[K^+]_{SC}$, although slower, results in a larger depolarization of the calyx. For these inputs to the VHCC model, both mechanisms together did not trigger spiking for smaller hair bundle deflections, but both were necessary to elicit spiking for the larger deflection. In the presence of an AP, the response of the model is influenced by currents at the hemi-nodes and nodes of the afferent fiber (*SI Appendix*, Eqs. **S6** and **S7** and Table S6). ϕ_C (Fig. 4*A*2) closely resembles experimental whole-cell recordings of the voltage response of a rat saccular calyx to positive step displacements (Songer and Eatock (9), their Fig. 5*A*).

The VHCC Model Captures the Frequency Response and Gain of NQT. Songer and Eatock (9) recorded responses from calyces in the excised rat saccule to sinusoidal hair bundle stimulation between 2 and 100 Hz in order to capture the frequency filtering characteristics relevant to natural head motions (1). An example of NQT from these experiments is reproduced in Fig. 5*A*. In addition to measuring the frequency-following capacity of the NQT-induced changes in calyx potential (ϕ_C), these data showed that for large bundle displacements NQT alone (without QT) can trigger APs in the afferent. Here we show the VHCC model's ability to reproduce these salient features of the experimental data and use the model to illustrate the roles of $[K^+]_{SC}$ and ϕ_{SC} in shaping the calyx response (Fig. 5).

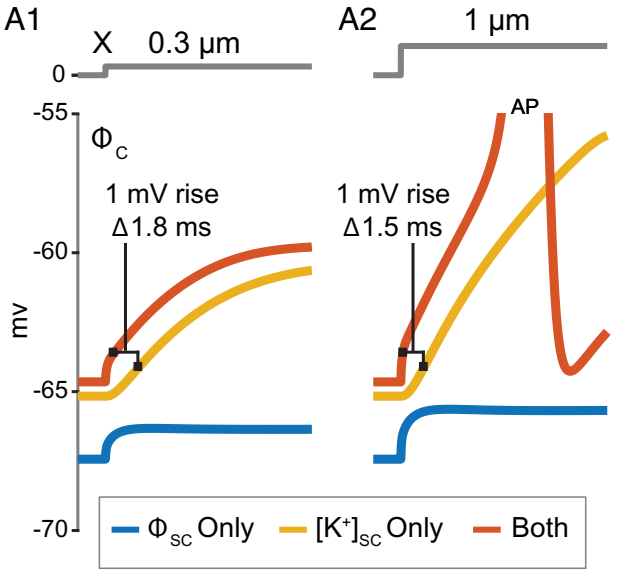

Fig. 4. ϕ_{SC} and $[K^+]_{SC}$ are responsible for the fast and slow components of NQT, respectively. (*A*1 and *A*2) Simulations of calyx potential ϕ_{SC} for two bundle displacement (X) steps (0.3 μm, 1 μm) with ϕ_{SC} modulation only (blue), with $[K^+]_{SC}$ modulation only (yellow) and with both enabled (dark orange).

The Model Captures NQT-driven Firing in Response to Sinusoidal Stimulus. The model produced calyx potentials that are consistent with whole-cell recordings (Fig. 5*A*), including spikes for large stimuli. In both data and model, the calyx was most likely to spike for stimulus frequencies between 10 and 50 Hz.

In Fig. 5 *B*–*E*, a small stimulus (±0.3 μm) was used to avoid triggering APs and better reveal the underlying changes in hair cell current and postsynaptic potential (ϕ_C). The model predicts that resistive currents ($I_{H,R}$) are much larger than capacitive currents ($I_{H,C}$) flowing from the type I hair cell (*SI Appendix*, Fig. S3). The capacitive current does increase with frequency, as expected, and can noticeably affect NQT during large voltage step stimuli (discussed later in Fig. 6).

Changes in Both ϕ_{SC} and $[K^+]_{SC}$ Are Required to Explain the Phase of the ϕ_C Response to Sinusoidal Stimuli. We examined the contribution of ϕ_{SC} and $[K^+]_{SC}$ to the phase of ϕ_H (Fig. 5*B*) and ϕ_C (Fig. 5*D*) as a function of frequency. A positive phase indicates that the maximal response of ϕ_H or ϕ_C is achieved before the maximal bundle displacement and is indicative of a high-pass filtering process. As shown, ϕ_{SC} contributes to a positive phase response in ϕ_H at frequencies below 32 Hz. For ϕ_H, at lower frequencies, the positive phase arises from $g_{K,L}$ activation (for kinetics, see *SI Appendix*, Table S6): during the depolarizing half cycle, an appreciable increase in $g_{K,L}$ (>10% at 2 Hz) produces an increasing outward current that truncates the rise in ϕ_H before the peak of the bundle displacement. Likewise, for ϕ_C the positive

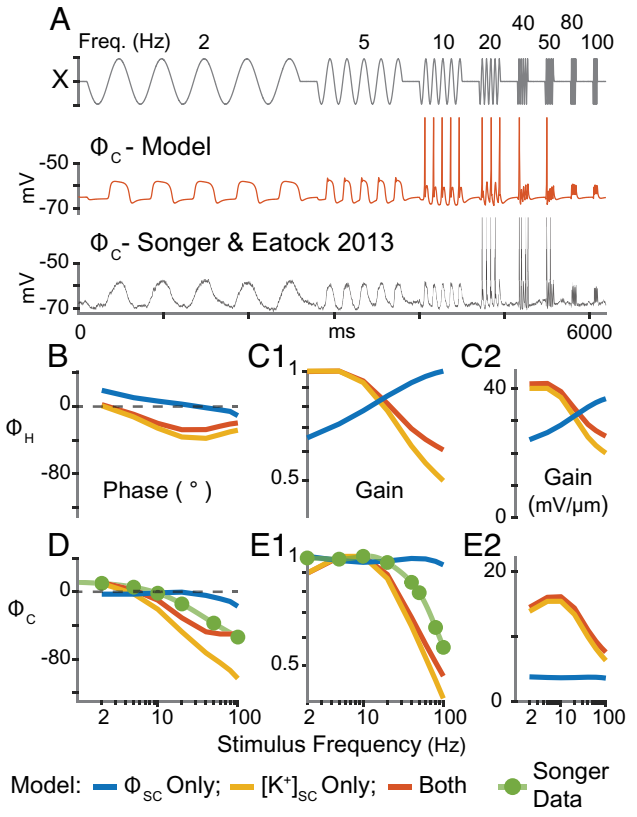

Fig. 5. Changes in ϕ_{SC} and $[K^+]_{SC}$ shape the phase and gain of the transmitted signal (ϕ_C). (*A*) Modeled ϕ_C response and whole-cell current-clamp recording of ϕ_C from rat saccular calyx (Songer and Eatock (9), their Fig. 5*B*) during ±1 μm sinusoidal bundle displacement. (*B*–*E*) Model outputs for ±0.3-μm bundle displacement analyzed into ϕ_{SC} modulation-only component (blue), $[K^+]_{SC}$ modulation-only component (yellow), and "Both" together (dark orange). Bode plots showing phase (*B*, *D*), normalized gain (*C*1 and *E*1) and gain (*C*2 and *E*2) of ϕ_H and ϕ_C relative to bundle displacement, X. (*D*) The contribution to the phase of ϕ_C from the $[K^+]_{SC}$ component (yellow) falls off much more steeply and with lower corner frequency than ϕ_{SC} component (blue). Combining them (dark orange) better matches experimental data [green, from Songer and Eatock (9), their Fig. 5*C*]. (*E*1 and *E*2) In the model, $[K^+]_{SC}$ modulation dominates the gain of NQT between 2 and 100 Hz, while ϕ_{SC} provides a small constant gain across a wide frequency band (blue, *E*2). Both components together produce slightly greater gain above 20 Hz (dark orange, *E*1).

phase at lower frequencies arises from activation of K_{LV} channels within the calyx and fiber. The ϕ_C response was nearly flat with frequency for the ϕ_{SC}-only condition but showed strong low-pass filtering for the $[K^+]_{SC}$-only component.

The low-pass behavior of $[K^+]$ modulation can be explained by the time course of K^+ accumulation or depletion in the cleft (*SI Appendix*, Eq. **S3**) and its effect on E_K, which is limited by the rate of K^+ entry through $g_{K,L}$, diffusion out of the cleft and flux across the calyx inner face membrane (11, 16). While the modulation of $[K^+]_{SC}$ is slow, the modulation of ϕ_{SC} is fast because it requires fewer ions than equivalent changes in E_K (*SI Appendix*, Notes). As a result, ϕ_{SC} rapidly changes both pre- and postsynaptic membrane voltages, altering both capacitive currents and resistive (ionic) currents through open channels. This explains the short response latency of ϕ_C at the onset of a step stimulus (Fig. 4). The ϕ_{SC} component is also required to closely approximate the phase of experimental data above 5 Hz (Fig. 5*D*). This effect supports the evidence from step data (Fig. 4) that a stimulus-modulated electrical potential in the synaptic cleft speeds up NQT.

$[K^+]_{SC}$ Dominates the Gain of NQT but ϕ_{SC} Slightly Boosts Gain at All Frequencies. Next, we examined the normalized and actual gain of averaged peak ϕ_H (Fig. 5 *C*1 and *C*2) and ϕ_C (Fig. 5 *E*1 and *E*2) as a function of frequency. For ϕ_H, the $[K^+]_{SC}$ mechanism contributes to a gain that rolls off above ~20 Hz, while the ϕ_{SC} mechanism linearly increases with frequency. Interestingly, the ϕ_{SC} mechanism kicks in to noticeably boost the ϕ_H gain above ~30 Hz. The crossover in ϕ_H gains resulting from changes in $[K^+]_{SC}$ and ϕ_{SC} shows that the impact of ϕ_{SC} increases with frequency. For ϕ_C, the gain at all frequencies is larger for the $[K^+]_{SC}$ component than for the ϕ_{SC} component (Fig. 5*E*2). The model also shows that the $[K^+]$ modulation mechanism amplifies the calyx potential response at all frequencies but especially below ~20 Hz. This effect is consistent with the increasing size of the $[K^+]_{SC}$ component relative to the ϕ_{SC} component with time during a displacement step (Fig. 4 *A*1 and *A*2). The ϕ_{SC} component is approximately constant with frequency, and the model predicts will boost the high-frequency gain (Fig. 5*E*1). However, the experimental ϕ_C gain (green) has a higher corner frequency (66 Hz) than the model output (36 Hz), which may reflect differences in afferent fiber properties between the model and specific experiments.

Paired Voltage Clamp Recordings from Hair Cell and Calyx Provide Evidence of Changes in Synaptic Cleft Potential. We have previously speculated that NQT involves the flow of K^+ through a large number of $g_{K,L}$ channels that are open at typical hair cell resting potentials (12). In this condition, receptor potentials instantaneously change K^+ current flowing into the synaptic cleft, bypassing the time—on the order of 1 to 100 ms—required to activate voltage-gated channels from the closed conformation. Experiments involving paired voltage-clamp recordings of whole-cell currents from turtle type I hair cells and postsynaptic calyces (18) address this hypothesis. In these experiments the hair cell was stepped to +20 mV from either –100 mV or –70 mV, while the calyx was held at either –100 mV or –70 mV, and fast inward calyx currents were recorded (Fig. 6 *A*1 and *A*2, respectively). At –70 mV (Fig. 6*A*2), currents were attributed to resistive coupling through presynaptic and postsynaptic ion channels open at the holding potential immediately prior to the voltage step. At –100 mV (Fig. 6*A*1), where calyceal K_{LV} channels are closed but HCN channels are open, fast currents were also visible.

The VHCC model was applied to analyze the experimental data with either the $[K^+]_{SC}$-only condition or the $[K^+]_{SC}$ *and* ϕ_{SC} ("Both") condition, described earlier. The fast postsynaptic currents only occurred in the "Both" condition (Fig. 6 *B*1 and *B*2), illustrating that changes in ϕ_{SC} were the primary driving force and that the recorded currents cannot be explained solely by changes in E_K. Under the "Both" condition, we first examined the model's output for a calyx and hair cell holding potential of –100 mV (Fig. 6 *C*1–*E*1). At this holding potential, $g_{K,L}$ and K_V7 channels were mostly closed and carried very little current prior to the voltage step. As ϕ_H is depolarized to +20 mV, ϕ_{SC} (Fig. 6*C*1) is primarily shaped by capacitive currents across the basolateral hair cell membrane ($I_{H,CAP}$) which precede $g_{K,L}$ activation (Fig. 6 *D*1 and *E*1). This variation in ϕ_{SC} alters V_{CIF}, shapes currents through the calyx inner face membrane (Fig. 6*B*1, asterisk), mostly via HCN2 channels (Fig. 6*E*1), and explains the recorded current (Fig. 6*A*1, asterisk). We identify these currents as evidence for changes in ϕ_{SC} in response to depolarization of the hair cell.

We then examined the model's output for calyx and hair cell holding potentials of –70 mV (Fig. 6, *Right* Column), where $g_{K,L}$ and K_V7 channels are significantly open prior to the voltage step. When ϕ_H is depolarized to +20 mV, ϕ_{SC} (Fig. 6*C*2) is primarily shaped by resistive currents through the basolateral hair cell membrane ($I_{H,R}$), mostly via $g_{K,L}$ (Fig. 6 *D*2 and *E*2). The change in ϕ_{SC} hyperpolarizes V_{CIF} (Fig. 6*C*2) and increases the inward driving force for currents through the calyx inner face, principally

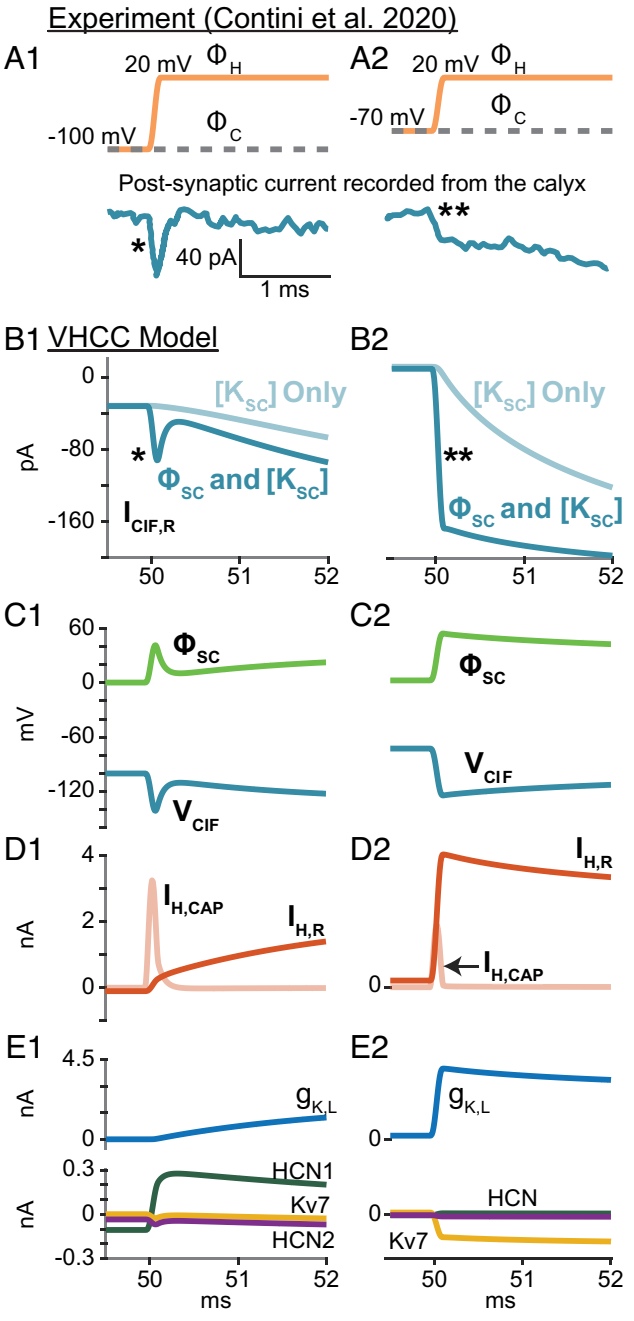

Fig. 6. Changes in synaptic cleft potential ϕ_{SC} explain the shape of fast postsynaptic currents in paired voltage recordings. (*A1* and *A2*) Voltage protocols and currents from experiment. (*A1*) Calyx Potential (ϕ_C) held at −100 mV. Hair cell potential stepped at 50 ms from holding potential of −100 to 20 mV. A2, Calyx Potential (ϕ_C) held at −70 mV. Hair cell potential stepped at 50 ms from holding potential of −70 to 20 mV. Currents reproduced from Contini et al. [(18), their Fig. 10]. (*B*–*E*) Model results. (*B1* and *B2*) Resistive postsynaptic current through the calyx inner face membrane ($I_{CIF,R}$) as calculated by the model. Note that fast currents (* and **) do not occur in the $[K]_{SC}$-only case (*faded blue*). Note similarities in shape (not magnitude) to recorded currents in *A1* and *A2*. (*C*) Electrical potential in the synaptic cleft (ϕ_{SC}) and voltage across the calyx inner face (V_{CIF}) membrane. (*C1*) The cleft potential is primarily shaped by capacitive currents from the hair cell ($I_{H,CAP}$, *D1*). (*C2*) The cleft potential is primarily shaped by resistive currents from the hair cell ($I_{H,R}$, *D2*). (*E*) Whole-cell currents through individual ion conductances. From the nonphysiological −100-mV holding potential (*A1*), HCN1 hair-cell current is prominent, fast, and sustained, because HCN channels are open at −100 mV (*E1*). Note that from −70-mV holding potential (*A2*), $g_{K,L}$ current is fast and sustained and K_V7 current (*yellow*) is the most prominent calyx current (*E2*). Currents through $g_{K,L}$ (*E2*) sustain the step in ϕ_{SC} following the voltage step in the hair cell. The slow decay reflects the change in driving force as K^+ accumulates in the cleft.

through K_V7 channels rather than HCN channels (Fig. 6*E2*), causing a fast current (double asterisks) similar in time course to the experimental record (18) (compare Fig. 6 *A2* and *B2*). The larger predicted amplitude of the fast current may reflect differences in key channel properties between the model parameters based on data from excised mouse and rat sacular epithelia with attached ganglia, and the experimental record, from excised turtle crista with attached brainstem. Based on the literature, key properties that differ across species or organs include the precise voltage dependence and size of $g_{K,L}$ and K_V7 and whether BK currents are evident in type I hair cells. For example, BK currents in type I hair cells have been implicated in NQT in the turtle crista (18), but were not detected in mouse utricle (34).

For depolarizing steps from both −70 and −100 mV (Fig. 6 *A1* and *A2*), the postsynaptic currents have a fast component and a slow component. These components are consistent with the existence of two driving forces with different time courses—ϕ_{SC} and E_K. Note that ϕ_{SC} (Fig. 6 *C1* and *C2*) follows the general shape of $\frac{d(\phi_H)}{dt}$ when capacitive currents dominate (at −100-mV holding potential, Fig. 6*D1*). In contrast, ϕ_{SC} (Fig. 6 *C1* and *C2*) follows the general shape of ϕ_H when resistive currents from the hair cell dominate (at −70-mV holding potential, Fig. 6*D2*, similar to reported hair cell resting potentials (~−80 to −60 mV, see *SI Appendix*, Table S4 for references). Under these physiological conditions, open $g_{K,L}$ channels (Fig. 6*E2*) are responsible for the changes in cleft potential and postsynaptic currents leading to both fast and sustained transmission of the hair cell receptor potential to the calyx (Fig. 6 *B2* and *C2*). These results show the importance for NQT of the unusual properties of $g_{K,L}$: together the large conductance and unusually negative half-activation voltage ensure that many hair cell channels are open near resting potential and ready to immediately respond to incoming stimuli. Interestingly, the model predicts that fast transmission can occur when $g_{K,L}$ is closed at −100 mV (Fig. 6*B1*). In this condition, capacitive coupling between the hair cell and the cleft changes ϕ_{SC} and V_{CIF} (Fig. 6*C1*), providing the driving force for a resistive current flow through HCN2 channels (Fig. 6*E1*) on the calyx inner face.

The predictions in Fig. 6 assume an ideal voltage clamp; the potential effects of series resistance are analyzed in the *SI Appendix*. Inclusion of series resistance and a model of $g_{K,L}$ that includes potassium relief of block (18) reduced the discrepancy between model predictions and experimental recordings at −70 mV (*SI Appendix*, Fig. S5).

NQT Depends on Calyx Morphology. The simulations we have presented are for a calyx shape typical of many calyces in the central and striolar zones of rodent vestibular epithelia (Fig. 1). However, calyces vary in their shape in different regions of amniote vestibular epithelia (30), and shorter "proto-calyces" are reported to exist in fish and amphibians (4, 44–47). To address the effects of calyx geometry on the two components (ϕ_{SC} and $[K^+]_{SC}$) of NQT, we studied both the steady-state condition and the step response (Fig. 7) for different calyx heights, while retaining the same ion channel and transporter expression per unit area of membrane. As the calyx was truncated (Fig. 7) to one-half or one-quarter of the height of our standard value for a rodent (11.33 μm) (Figs. 1 and 7, "Calyx"), both ϕ_{SC} and $[K^+]_{SC}$ were closer to perilymph values (0 mV and 5 mM, respectively) at rest (Fig. 7 *A* and *D*), had smaller responses to stimuli (Fig. 7 *B* and *E*), and no spikes were initiated in the afferent fiber. However, the model does suggest that the truncated calyces could accumulate enough K^+ (Fig. 7*F*) to facilitate afferent depolarization. The effect on ϕ_C at the onset of bundle stimulation is small, ~2 mV

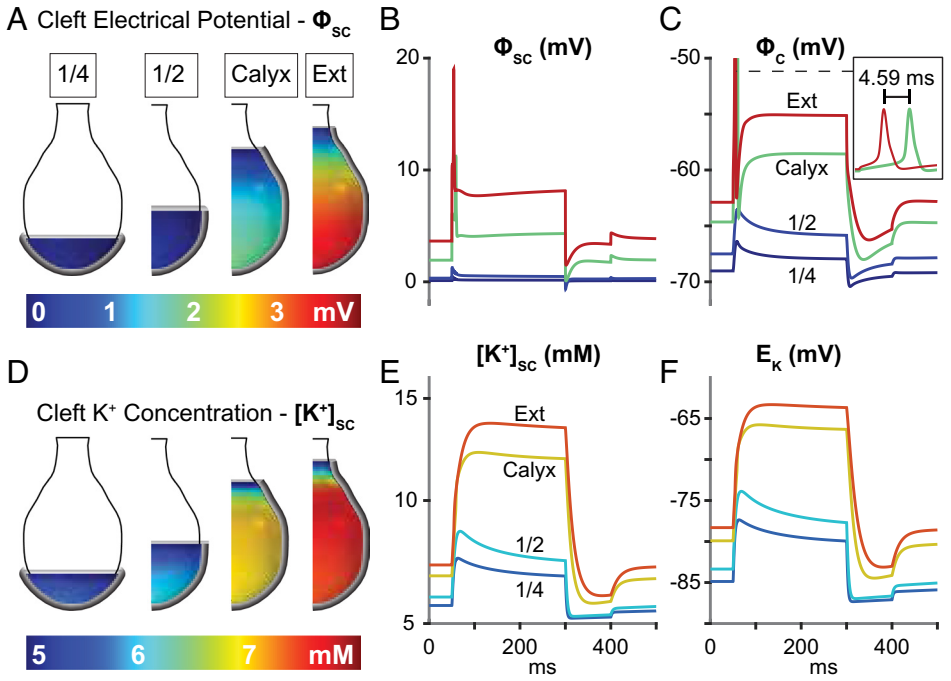

Fig. 7. Magnitude and speed of NQT increase with calyx height. (*A* and *D*) The 3D visualizations represent a shell the width of the cleft space resting between the hair cell and calyx. Silver edges delineate calyces of different heights. Spatial gradients of ϕ_{SC} and $[K^+]_{SC}$ are visible within these regions. The outer surface of the hair cell above the calyx is exposed to perilymph (ϕ = 0 mV, ground and [K^+] = 5 mM). (*B*, *C*, *E*, and *F*) Changes in ϕ_{SC}, ϕ_C, $[K^+]_{SC}$ and E_K increase with calyx height. Curve colors correspond to those at the base of each calyx in *A* and *D* at steady state. (*A*) The spatial distribution of ϕ_{SC} at rest as a function of calyx height. (*B*) ϕ_{SC} at the base of the synapse over the course of step bundle displacement (same as in Fig. 2*A*). (*C*) Changes in ϕ_C (the transmitted signal). The inset demonstrates the reduction in time to spike as calyx height is increased by 2 μm from 11.3 to 13.3 μm. (*D*) The spatial distribution of $[K^+]_{SC}$ at rest. (*E*) $[K^+]_{SC}$ at the base of the synapse over the course of step bundle displacement. (*F*) E_K values corresponding to changes in $[K^+]_{SC}$. Compare with ϕ_{SC} (*B*).

(Fig. 7*C*). On the other hand, increasing calyx height by 2 μm (Fig. 7, "Ext") increased ϕ_{SC} and $[K^+]_{SC}$ at rest, increased rate and magnitude of stimulus-evoked changes in ϕ_C, and reduced transmission latency (Fig. 7*C*). The greater calyx height is found in "dimorphic" afferents (30), which have both calyx and bouton endings.

Fig. 7 shows that increasing calyx height and thereby extending the synaptic cleft increases resting values of ϕ_{SC} and $[K^+]_{SC}$, depolarizes both hair cell and calyx potentials, opens more ion channels at rest, increases stimulus-evoked changes in both ϕ_{SC} and $[K^+]_{SC}$, increases the likelihood of postsynaptic spiking, and reduces first-spike latency (Fig. 7*C*; a calyx spike is evident in ϕ_{SC} traces for the standard and extended calyx). Simulations of calyx heights at finer intervals indicated that NQT-initiated spiking required a calyx height within 95% of our standard value (11.3 μm), suggesting that the central-zone calyx has the minimal height required for NQT-driven spiking. Once this minimal height is achieved, further increases raise the magnitude and rate of NQT and reduce the time-to-spike, reflecting increases in the calyceal membrane area, the extent of the synaptic cleft, axial resistance, and the distance to perilymph at the calyx apex.

Discussion

We have constructed a biophysical model that incorporates ultrastructural data on the geometry of the VHCC synapse, immunocytochemical data on the expression of ion channels and transporters, and electrophysiological data on kinetics of ion channels. Our goal was to understand the mechanism of NQT at the unique VHCC synapse, which is characterized by its extensive and unfenestrated synaptic cleft, and the many low-voltage-activated potassium (K_{LV}) channels that populate the pre- and postsynaptic membranes. The model predicts dynamic changes in the potassium concentration $[K^+]_{SC}$ and electrical potential ϕ_{SC} in the synaptic cleft in response to hair bundle deflection or paired voltage-clamp recordings, which explain experimental recordings of both fast (9, 18) and slow (10, 11) NQT. In the process, we were able to identify three salient features in existing experimental recordings that support the existence of an electrical potential in the synaptic cleft and its role in NQT: the frequency dependence of the phase of NQT (Fig. 5*D*) (9); the fast retrograde events in hair cell potential during retrograde transmission of postsynaptic spikes (Fig. 3, see asterisks) (11); and the shape of fast postsynaptic currents (Fig. 6) (18).

The VHCC model permits a clear description of the sequence of events that constitute NQT, shown in Figs. 2 and 3. Modulation of hair cell potential immediately changes the synaptic cleft potential ϕ_{SC} and gradually changes the potassium potential E_K. During physiological operation, both are primarily accomplished by change in a large K^+ current through the noninactivating, low-voltage-activated potassium conductance, $g_{K,L}$, on the hair cell basolateral membrane. The properties of $g_{K,L}$ suit its role in NQT. First, $g_{K,L}$ is >50% open at the hair cell resting potential, allowing the receptor potential to immediately alter membrane current and thereby ϕ_{SC}. Second, $g_{K,L}$ is noninactivating, ensuring that significant K^+ will accumulate in the cleft during sustained or low-frequency hair cell stimulation. We also considered the proposal that cleft K^+ modulates $g_{K,L}$ activation by relieving channel block (18). For the physiological voltage changes evoked by a large hair bundle stimulus, our Hodgkin–Huxley modeling of $g_{K,L}$ captured the recorded behavior well (Fig. 5). Implementing K^+ relief of block to describe $g_{K,L}$ activation generated comparable results

(*SI Appendix,* Notes and Fig. S4). However, the K^+ relief of block model provides more accurate predictions for experiments involving large voltage excursions (*SI Appendix*, Fig. S5).

The changes in cleft electrical and K^+ potentials alter the driving forces of currents across the calyx inner face, which contains a large number of noninactivating, low-voltage-activated channels (K_V7) that are significantly open at rest (~30%). Upon stimulation, increases in ϕ_{SC} and $[K^+]_{SC}$ reduce the outward K_V7 current and depolarize the calyx. In short, the presence of open K_{LV} channels in the pre- and postsynaptic membranes enables NQT as previously proposed (12, 19). The VHCC model clarifies the role of ϕ_{SC} and E_K as separate driving forces for currents through all channels facing the synaptic cleft. The fast components of NQT are transmitted via the modulation of ϕ_{SC} and the slow components via $[K^+]_{SC}$.

The cleft electrical potential (ϕ_{SC}) improves the ability of both the hair cell and calyx to follow sinusoidal stimuli at higher frequencies (Fig. 5 *B*–*E*). Consistent with this prediction, fast postsynaptic currents observed following instantaneous voltage steps (Fig. 6) are also driven by changes in ϕ_{SC} caused by capacitive and resistive currents from the hair cell (Fig. 6 *D* and *E*). The VHCC model identifies the hair cell, cleft, and calyx as three compartments in series. Given that resistive currents between any two compartments (hair cell and cleft; cleft and calyx) are driven by both electrical potential and ion concentration gradients, resistive coupling contributes to both fast and slow components of NQT. Capacitive coupling contributes exclusively to the fast NQT component by rapidly altering the cleft electrical potential. Predictably, capacitive currents from the hair cell increase with frequency during bundle stimulation (*SI Appendix*, Fig. S3), and are prominent during voltage steps from voltages where $g_{K,L}$ is closed (Fig. 6*C*1). Both resistive and capacitive coupling are observed in other systems where neural membranes are held in close proximity by specialized structures, such as the Mauthner cell axon cap and the basket cell's pinceau terminal on a Purkinje cell (6).

At the calyx of Held, a large presynaptic calyx important for auditory processing, analysis of ephaptic coupling (48) suggests that although presynaptic capacitive and resistive currents occur, the fenestrations in the calyx of Held reduce synaptic cleft potentials, ensuring that presynaptic calcium channels sense the full presynaptic AP and rapidly initiate neurotransmitter release. In contrast, the VHCC model shows that the unfenestrated morphology of the calyx increases cleft $[K^+]_{SC}$ and ϕ_{SC}, complementary mechanisms that mediate NQT. The slower change in $[K^+]_{SC}$ increases the gain of NQT for slow or sustained hair bundle deflections, while the near-instantaneous change in ϕ_{SC} enables the calyx to closely follow dynamic hair cell potentials and explains the calyx-bearing afferent's short latency and ability to follow relatively high-stimulus frequencies, including sound and vibration (5, 9, 18, 27). The calyx is essential for both fast and slow NQT, and as calyx height increases, the efficacy of both mechanisms increases and transmission latency decreases.

These findings explain the exceptional speed of neurotransmission between type I hair cells and vestibular afferents, which is even faster than the QT between cochlear hair cells and afferents (5). At its fastest, QT imposes a 0.4 to 0.6-ms delay (49), reflecting the time required for multiple steps from the opening of presynaptic voltage-gated calcium channels to the opening of postsynaptic neurotransmitter-gated receptor channels. For fast vestibular reflexes, with latencies as short as 5 ms between head motion and motor response (50), a mechanism that avoids the synaptic delay of quantal release is a significant advantage. Our results show that robust NQT, enabled by the evolution of the full calyx, substantially reduces the latency and advances the phase of vestibular signals that drive neural circuits controlling gaze, balance, and orientation.

While we have focused on NQT, type I vestibular hair cells have ribbon synapses that coordinate vesicle release of glutamate into the synaptic cleft (28) in a process dependent on activation of voltage-gated calcium ($Ca_V1.3$) channels. Glutamate transiently activates AMPA receptors on the calyx inner face and may also accumulate in the cleft to influence the slow phase of NQT and to broaden quantal EPSCs (20). In our model, the hair cell membrane depolarizes to -62 mV (at the base) (Fig. 2 *D* and *D*1) and -58 mV (toward the cleft opening) during bundle displacement, these voltages correspond to $Ca_V1.3$ channel open probabilities of just 4 to 8%. This may not reflect the situation in vivo; e.g., the MET conductance we used in the VHCC model is based on recordings in 1.3 mM external $[Ca^{2+}]$. However, vestibular endolymph has only 100 to 200 μM Ca^{2+} (51) and external Ca^{2+} blocks MET channels (52), such that the MET conductance and therefore both NQT and QT may be larger in vivo. On the other hand, type I vestibular hair cells have relatively small Ca^{2+} currents and quantal release compared with other hair cells (53). Our results agree with evidence that 1) NQT alone can elicit afferent spikes (9) and 2) NQT reduces the number of quanta necessary to elicit APs in the afferent (11). When QT and NQT occur together, they filter the incoming signal in different ways (9), but how the combined information is handled centrally is not understood.

In conclusion, the VHCC model provides a quantitative description of NQT and describes two parallel paths for NQT across the synaptic cleft: changing the cleft electrical potential and changing the potassium potential. It also delineates the roles of specific ion channels and calyx geometry in NQT. In contrast to experiments that can only calculate the effective $[K^+]_{SC}$ based on whole-cell currents, the model is able to predict the gradients that must occur in both $[K^+]_{SC}$ and ϕ_{SC} along the extent of the cleft. This capability offers promise for investigating channel microdomains (30) at the VHCC synapse. Here we have focused on NQT in a simple calyx from central or striolar zones of vestibular epithelia; the model can be extended to explore QT and the functional effects of other afferent terminal forms, such as the complex calyces that enwrap multiple type I hair cells and the elaborate dimorphic terminal arbors that include calyces and boutons (reviewed in refs. 4, 54 and 55).

Methods

Computational Methods. To investigate NQT, model simulations were performed using a finite element geometry representative of the vestibular hair cell and calyx in COMSOL Multiphysics software. The general setup of the model, the modeling of membrane currents, the governing equations for electrical potentials and ion concentrations, solver conditions, and channel distributions and kinetics are fully described in the *SI Appendix*.

Experimental Methods. Whole-cell patch-clamp recordings were performed on mouse vestibular afferent neurons to measure the activation and inactivation time constants of the Na_V current. Confocal microscopy and immunocytochemistry were performed to study the localization of KCC, the relative density of Kv7.4, and the morphology of the VHCC synapse. Experimental details are fully described in *SI Appendix*.

Data, Materials, and Software Availability. The model was implemented in Comsol Multiphysics 5.6 software. Equations and data sources are available in *SI Appendix*, Computational Methods and Experimental Methods. The Comsol file (.mph) containing the model, and other supporting files, are publicly publicly available on GitHub: (https://github.com/acgsci/vestibularHairCellCalyxNQT).

ACKNOWLEDGMENTS. This study was supported by NIH (R01 DC012347 and DC002290), an Emerging Research Grant from the Hearing Health Foundation and a seed grant from the Rice University ENRICH program. We are grateful to Hannah Martin and Oleg Igoshin for stimulating discussions and Selina Baeza-Loya for providing activation and inactivation time constants of afferent voltage-gated sodium channels.

Author affiliations: [a]Applied Physics Graduate Program, Smalley-Curl Institute, Rice University, Houston, TX 77005; [b]Department of Bioengineering, Rice University, Houston, TX 77005; [c]Department of Neurology, Yale University School of Medicine, New Haven, CT 06510; [d]Department of Anatomy and Cell Biology, University of Illinois at Chicago, Chicago, IL 60612; and [e]Department of Neurobiology, University of Chicago, Chicago, IL 60637

1. K. E. Cullen, Vestibular processing during natural self-motion: Implications for perception and action. *Nat. Rev. Neurosci.* **20**, 346–363 (2019).
2. J. Wersäll, Studies on the structure and innervation of the sensory epithelium of the cristae ampulares in the guinea pig; a light and electron microscopic investigation. *Acta. Otolaryngol. Suppl.* **126**, 1–85 (1956).
3. R. L. Gulley, D. Bagger-Sjöbäck, Freeze-fracture studies on the synapse between the type I hair cell and the calyceal terminal in the guinea-pig vestibular system. *J. Neurocytol.* **8**, 591–603 (1979).
4. A. Lysakowski, J. M. Goldberg, "Morphophysiology of the vestibular periphery" in *Springer Hearing and Auditory Research*, S. M. Highstein, R. R. Fay, A. N. Popper, Eds. (Springer New York, 2004), pp. 57–152.
5. M. McCue, J. Guinan, Acoustically responsive fibers in the vestibular nerve of the cat. *J. Neurosci.* **14**, 6058–6070 (1994).
6. D. S. Faber, A. E. Pereda, Two forms of electrical transmission between neurons. *Front. Mol. Neurosci.* **11**, 427 (2018).
7. M. Yamashita, H. Ohmori, Synaptic responses to mechanical stimulation in calyceal and bouton type vestibular afferents studied in an isolated preparation of semicircular canal ampullae of chicken. *Exp. Brain. Res.* **80**, 475–488 (1990).
8. J. C. Holt, S. Chatlani, A. Lysakowski, J. M. Goldberg, Quantal and nonquantal transmission in calyx-bearing fibers of the turtle posterior crista. *J. Neurophysiol.* **98**, 1083–1101 (2007).
9. J. E. Songer, R. A. Eatock, Tuning and timing in mammalian type I hair cells and calyceal synapses. *J. Neurosci.* **33**, 3706–3724 (2013).
10. S. M. Highstein, G. R. Holstein, M. A. Mann, R. D. Rabbitt, Evidence that protons act as neurotransmitters at vestibular hair cell–calyx afferent synapses. *Proc. Natl. Acad. Sci. U.S.A.* **111**, 5421–5426 (2014).
11. D. Contini, S. D. Price, J. J. Art, Accumulation of K^+ in the synaptic cleft modulates activity by influencing both vestibular hair cell and calyx afferent in the turtle. *J. Physiol.* **595**, 777–803 (2017).
12. R. A. Eatock, Specializations for fast signaling in the amniote vestibular inner ear. *Integr. Comp. Biol.* **58**, 341–350 (2018).
13. R. A. Eatock, A. Lysakowski, "Mammalian Vestibular Hair Cells" in Vertebrate Hair Cells, R. A. Eatock, R. R. Fay, A. N. Popper, Eds. (Springer New York, 2006), pp. 348–442.
14. J. W. Y. Chen, "*The properties and functions of a low-voltage K+ current in type I hair cells of rat semicircular canal organs*," University of Rochester, Rochester, NY. (1995).
15. J. M. Goldberg, Theoretical analysis of intercellular communication between the vestibular type I hair cell and its calyx ending. *J. Neurophysiol.* **76**, 1942–1957 (1996).
16. R. Lim, A. E. Kindig, S. W. Donne, R. J. Callister, A. M. Brichta, Potassium accumulation between type I hair cells and calyx terminals in mouse crista. *Exp. Brain Res.* **210**, 607–621 (2011).
17. D. Contini *et al.*, Intercellular K^+ accumulation depolarizes type I vestibular hair cells and their associated afferent nerve calyx. *Neuroscience* **227**, 232–246 (2012).
18. D. Contini, G. R. Holstein, J. J. Art, Synaptic cleft microenvironment influences potassium permeation and synaptic transmission in hair cells surrounded by calyx afferents in the turtle. *J. Physiol.* **598**, 853–889 (2020).
19. P. Spaiardi *et al.*, K^+ accumulation and clearance in the calyx synaptic cleft of type I mouse vestibular hair cells. *Neuroscience* **426**, 69–86 (2020).
20. S. G. Sadeghi, S. J. Pyott, Z. Yu, E. Glowatzki, Glutamatergic signaling at the vestibular hair cell calyx synapse. *J. Neurosci.* **34**, 14536–14550 (2014).
21. J. G. Jefferys, Nonsynaptic modulation of neuronal activity in the brain: Electric currents and extracellular ions. *Physiol. Rev.* **75**, 689–723 (1995).
22. R. Vroman, L. J. Klaassen, M. Kamermans, Ephaptic communication in the vertebrate retina. *Front. Hum. Neurosci.* **7**, 612 (2013).
23. T. J. Warren, M. J. Van Hook, D. Tranchina, W. B. Thoreson, Kinetics of inhibitory feedback from horizontal cells to photoreceptors: Implications for an ephaptic mechanism. *J. Neurosci.* **36**, 10075–10088 (2016).
24. K.-S. Han, C. H. Chen, M. M. Khan, C. Guo, W. G. Regehr, Climbing fiber synapses rapidly and transiently inhibit neighboring Purkinje cells via ephaptic coupling. *Nat. Neurosci.* **23**, 1399–1409 (2020).
25. C. Chiang, R. S. Shivacharan, X. Wei, L. E. Gonzalez-Reyes, D. M. Durand, Slow periodic activity in the longitudinal hippocampal slice can self-propagate non-synaptically by a mechanism consistent with ephaptic coupling. *J. Physiol.* **597**, 249–269 (2019).
26. R. G. Gourdie, The cardiac gap junction has discrete functions in electrotonic and ephaptic coupling. *Anat. Rec.* **302**, 93–100 (2019).
27. I. S. Curthoys *et al.*, A review of mechanical and synaptic processes in otolith transduction of sound and vibration for clinical VEMP testing. *J. Neurophysiol.* **122**, 259–276 (2019).
28. A. Lysakowski, J. M. Goldberg, A regional ultrastructural analysis of the cellular and synaptic architecture in the chinchilla cristae ampullares. *J. Comp. Neurol.* **389**, 419–443 (1997).
29. A. Lysakowski, J. M. Goldberg, Ultrastructural analysis of the cristae ampullares in the squirrel monkey (Saimiri sciureus). *J. Comp. Neurol.* **511**, 47–64 (2008).
30. A. Lysakowski *et al.*, Molecular microdomains in a sensory terminal, the vestibular calyx ending. *J. Neurosci.* **31**, 10101–10114 (2011).
31. I. H. Quraishi, "*Computational modeling of potassium transport in the inner ear*," Rice University, Houston, TX. (2008)
32. K. J. Rennie, M. J. Correia, Potassium currents in mammalian and avian isolated type I semicircular canal hair cells. *J. Neurophysiol.* **71**, 317–329 (1994).
33. K. J. Rennie, A. J. Ricci, M. J. Correia, Electrical filtering in gerbil isolated type I semicircular canal hair cells. *J. Neurophysiol.* **75**, 2117–2123 (1996).
34. A. Rüsch, R. A. Eatock, A delayed rectifier conductance in type I hair cells of the mouse utricle. *J. Neurophysiol.* **76**, 995–1004 (1996).
35. J. W. Y. Chen, R. A. Eatock, Major potassium conductance in type I hair cells from rat semicircular canals: Characterization and modulation by nitric oxide. *J. Neurophysiol.* **84**, 139–151 (2000).
36. P. Spaiardi *et al.*, An allosteric gating model recapitulates the biophysical properties of $I_{K,L}$ expressed in mouse vestibular type I hair cells: Allosteric gating of $I_{K,L}$. *J. Physiol.* **595**, 6735–6750 (2017).
37. E. Soto, R. Vega, R. Budelli, The receptor potential in type I and type II vestibular system hair cells: A model analysis. *Hear. Res.* **165**, 35–47 (2002).
38. D. Johnston, *Foundations of cellular neurophysiology* (MIT Press, 1995), pp. 12–13.
39. M. J. Correia, D. G. Lang, An electrophysiological comparison of solitary type I and type II vestibular hair cells. *Neurosci. Lett.* **116**, 106–111 (1990).
40. K. M. Hurley *et al.*, M-like K^+ currents in type I hair cells and calyx afferent endings of the developing rat utricle *J. Neurosci.* **26**, 10253–10269 (2006).
41. G. C. Horwitz, J. R. Risner-Janiczek, S. M. Jones, J. R. Holt, HCN channels expressed in the inner ear are necessary for normal balance function. *J. Neurosci.* **31**, 16814–16825 (2011).
42. G. C. Horwitz, J. R. Risner-Janiczek, J. R. Holt, Mechanotransduction and hyperpolarization-activated currents contribute to spontaneous activity in mouse vestibular ganglion neurons. *J. Gen. Physiol.* **143**, 481–497 (2014).
43. J. C. Holt *et al.*, Muscarinic acetylcholine receptors and M-currents underlie efferent-mediated slow excitation in calyx-bearing vestibular afferents. *J. Neurosci.* **37**, 1873–1887 (2017).
44. V. Honrubia, L. F. Hoffman, S. Sitko, I. R. Schwartz, Anatomic and physiological correlates in bullfrog vestibular nerve. *J. Neurophysiol.* **61**, 688–701 (1989).
45. P. J. Lanford, A. N. Popper, Novel afferent terminal structure in the crista ampullaris of the goldfish, carassius auratus. *J. Comp. Neurol.* **366**, 572–579 (1996).
46. R. Boyle, R. Ehsanian, A. Mofrad, Y. Popova, J. Varelas, Morphology of the utricular otolith organ in the toadfish, Opsanus tau. *J. Comp. Neurol.* **526**, 1571–1588 (2018).
47. O. Lowenstein, M. P. Osborne, R. A. Thornhill, The anatomy and ultrastructure of the labyrinth of the lamprey (Lampetra fluviatilis L.). *Proc. R. Soc. Lond. B Biol. Sci.* **170**, 113–134 (1968).
48. M. C. Sierksma, J. G. G. Borst, Using ephaptic coupling to estimate the synaptic cleft resistivity of the calyx of Held synapse. *PLoS Comput. Biol.* **17**, e1009527 (2021).
49. J. E. Lisman, S. Raghavachari, R. W. Tsien, The sequence of events that underlie quantal transmission at central glutamatergic synapses. *Nat. Rev. Neurosci.* **8**, 597–609 (2007).
50. M. Huterer, K. E. Cullen, Vestibuloocular reflex dynamics during high-frequency and high-acceleration rotations of the head on body in rhesus monkey. *J. Neurophysiol.* **88**, 13–28 (2002).
51. A. N. Salt, N. Inamura, R. Thalmann, A. Vora, Calcium gradients in inner ear endolymph. *Am. J. Otolaryngol.* **10**, 371–375 (1989).
52. A. J. Ricci, R. Fettiplace, Calcium permeation of the turtle hair cell mechanotransducer channel and its relation to the composition of endolymph. *J. Physiol.* **506**, 159–173 (1998).
53. P. Spaiardi, W. Marcotti, S. Masetto, S. L. Johnson, Signal transmission in mature mammalian vestibular hair cells. *Front. Cell Neurosci.* **16**, 806913 (2022).
54. J. M. Goldberg, Afferent diversity and the organization of central vestibular pathways. *Exp. Brain Res.* **130**, 277–297 (2000).
55. R. A. Eatock, J. E. Songer, Vestibular hair cells and afferents: Two channels for head motion signals. *Annu. Rev. Neurosci.* **34**, 501–534 (2011).